Experiments in Fluids (2024) 65:120
https://doi.org/10.1007/s00348-024-03859-0

RESEARCH ARTICLE

Temperature imaging during the hydrogen release reaction from a liquid organic hydrogen carrier (LOHC) system using phosphor thermometry

Jonas Bollmann[1,2] · Florian Bauer[1,2] · Silvan Keim[1] · Nikolas Herz[4] · Lars Zigan[1,2,3] · Peter Wasserscheid[4,5,6] · Stefan Will[1,2]

Received: 29 February 2024 / Revised: 17 July 2024 / Accepted: 18 July 2024 / Published online: 5 August 2024

Abstract

Liquid organic hydrogen carrier (LOHC) systems offer a particularly interesting option for chemical hydrogen storage. In order to characterize and understand the endothermal hydrogen release from the carrier liquid and to evaluate suitable catalyst materials, knowledge of the temperature fields in the dehydrogenation reactor is important. One suitable technique for planar temperature sensing in reacting systems is phosphor thermometry. It is based on the excitation of a luminescent material by a laser pulse and detection of the subsequent phosphorescence signal. We investigated the luminescence of the thermographic phosphor (Sr,Ca)$SiAlN_3$:Eu^{2+} ("SCASN:Eu^{2+}") dispersed in the H0-DBT / H18-DBT LOHC system in a temperature range from 400 to 600 K. A measurement cell enables repeatable and homogeneous measurement conditions of the hydrogen release reaction. A catalytic plate was put inside the heated LOHC. Temperature fields during the hydrogen release reaction were measured for the first time using the phosphorescence decay time (PDT) and the phosphorescence intensity ratio method (PIR). As expected, a strong cooling at the catalyst surface during the endothermal hydrogen release reaction could be observed, which was quantified to be in the range of 40 K.

Graphical abstract

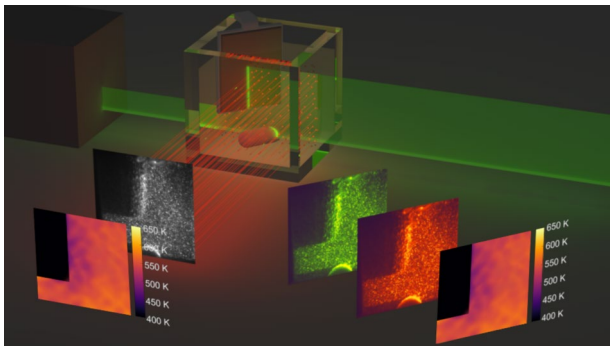

1 Introduction

For many applications related to chemical reactions, detailed information about temperature is crucial (Childs et al. 2000). One such example is the storage of hydrogen using liquid organic hydrogen carrier (LOHC) systems (Teichmann et al. 2012). LOHC systems are composed of at least one hydrogen-lean and one corresponding hydrogen-rich molecule. An exothermic catalytic hydrogenation reaction binds hydrogen to the lean LOHC molecule, which is thereby transformed into its hydrogen-rich counterpart that can be safely stored at ambient conditions for long time periods. An endothermic dehydrogenation reaction–also in presence of a catalyst–is used to release hydrogen from the hydrogen-rich LOHC molecule (Preuster et al. 2017a). The thermal stability of all LOHC components is important for their repetitive use in hydrogenation/dehydrogenation cycles (Preuster et al.

Extended author information available on the last page of the article

2017b). Here, it is essential to know the actual temperature fields in the reactor and to control them as this is ultimately related to the efficiency and technical durability of the system. Further, the development of efficient catalyst materials requires a detailed understanding about their performance. Knowledge about the temperature distribution close to the reactive surface is one key aspect for such evaluation. Another important aspect is the fact that hot spots in the reactor may lead to degradation of the recyclable carrier molecules limiting their lifetime and durability. Here, fixed-positioned pointwise thermocouple detectors do often not sufficiently localize such thermal hotspots and instead imaging techniques are desirable.

In recent years, the LOHC system dibenzyltoluene (H0-DBT)/ perhydro dibenzyltoluene (H18-DBT) has emerged as particularly relevant for industrial applications due to its advantageous properties (Bollmann et al. 2022; Bruckner et al. 2014; Preuster, et al. 2017a; Teichmann et al. 2011). The DBT-based system has a good hydrogen storage capacity of 6.2 mass %, a high thermal stability and excellent commercial availability. Additionally, the high boiling point of 663 K and the high flashpoint of 473 K result in a simplified LOHC handling and good intrinsic safety of this storage system (Modisha and Bessarabov 2020; Preuster, et al. 2017a). An overview of the hydrogen storage cycle with the H0-DBT/ H18-DBT LOHC system can be found in (Bollmann, et al. 2022; Preuster, et al. 2017b). The temperatures of interest during the dehydrogenation process of the LOHC system H0-DBT/ H18-DBT range between 450 and 600 K and measurement techniques for their determination are required for a comprehensive understanding of the thermal behavior and hydrogen release.

For the determination of temperature fields in fluid flows the use of thermographic luminescent materials has been established as a favorable method. These are added to a fluid in a suitable way, and the temperature-dependence of the emission behavior after excitation by a laser pulse is exploited, either making use of its temporal or spectral characteristics. Thermographic luminescent materials are used in many different forms, including molecular tagging thermometry (MTT) (Khalid and Kontis 2008), luminescence nanothermometry (van Swieten et al. 2021), laser-induced fluorescence (LIF) (Lemoine and Castanet 2013; Schulz and Sick 2005)with an overview about advantages and limitations of each technique provided in (Abram et al. 2018; Someya 2021). This work focuses on the use of thermographic phosphors. Here, combined measurements of temperature and velocity in gaseous or liquid flows are possible. Further, a wide temperature range and the inert behavior of the phosphors lead to a broad range of possible applications (Beyrau et al. 2021; Dramićanin 2020; Someya 2021).

Previous studies on phosphor thermometry in liquids were performed with BAM:Eu^{2+} (Lindén et al. 2012), SMP:Sn^{2+} (Fond et al. 2019b), MFG:Mn^{4+} (Brübach et al. 2006; Fond et al. 2019a; Kim et al. 2017), $ScVO_4$:Bi^{3+} (Abram et al. 2020) and ZnO (Abram et al. 2016) with an overview provided in a previous study (Bollmann et al. 2023). Unfortunately, none of the presented TSPs and phosphors meet the requirements with respect to measurements in reacting and often transient LOHC systems, as they either show strong absorption of the utilized excitation wavelengths by the LOHC or too long decay times hindering sufficient time resolution. Recently, Hertle et al. have investigated the temperature-dependent properties of the phosphor (Sr,Ca)$SiAlN_3$:Eu^{2+} (SCASN:Eu^{2+}) for studying thermometry of solid bulk and coated materials (Hertle et al. 2020). The absorption and emission characteristics of this phosphor appear to be well suited for temperature measurements in the H0-DBT/ H18-DBT LOHC system. In a previous work of the authors (Bollmann, et al. 2023) SCASN:Eu^{2+} was characterized with respect to its suitability for phosphor thermometry in heat transfer fluids and non-reacting LOHC systems comparing the pointwise PIR and PDT method.

The aim of this work is to measure temperature fields during the endothermic hydrogen release from H18-DBT using the phosphor SCASN:Eu^{2+} and the PDT and PIR method. During this reaction, local temperatures must be known and controlled precisely in order to make full use of the available reactor volume, while avoiding overheating that would lead to thermal decomposition of the liquid carrier. Exact knowledge of the temperature field around the active catalytic surface is key to evaluate the performance of different dehydrogenation catalysts. An important aspect here is the localization of cool spots near the catalyst surface in the LOHC in order to provide the required enthalpy and temperature for the reaction in this specific area. As the efficiency of the dehydrogenation reaction strongly depends on the local temperature level (Dürr et al. 2021; Willer et al. 2024), its actual knowledge would be extremely helpful to follow dehydrogenation on a microscopic level. A provision of experimentally obtained temperatures would also be extremely helpful for future detailed simulations of this process. Against this background, we calibrate the planar PDT method based on SCASN:Eu^{2+} in the LOHC-system H0- DBT/ H18- DBT using a calibration cell. In the second step we use an optically accessible model dehydrogenation reactor to resolve temperature fields during the hydrogen release reaction using H18-DBT.

2 Theory of phosphor thermometry

The temporal and spectral characteristics of the phosphorescence emission signal of thermographic phosphors mainly depend on temperature. The temperature dependent decay time of an excited phosphor is a result of the

probability of nonradiative relaxation processes (Eldridge 2019). With increasing temperature, higher energy levels in the crystal lattice are populated, which increases the probability of nonradiative decay processes. The increase in the rate of non-radiative transitions results in a faster depopulation of the excited state and therefore a shorter phosphorescence lifetime (Abram, et al. 2018). Typically, also the phosphorescence quantum yield is reduced above a certain quenching temperature.

Equation (1) shows the emission intensity I over time t after a short excitation, resulting in a monoexponential decay behavior with a characteristic temperature dependent decay time $\tau(T)$ (Fuhrmann et al. 2014),

$$I(t) = I_0 \cdot \mathrm{e}^{-\frac{t}{\tau(T)}} + b. \tag{1}$$

After eliminating the offset intensity b, the decay time τ is the time period in which the emission signal intensity $I(t)$ decreases to the fraction e^{-1} of its initial value I_0 and can be further described by (Dramićanin 2018)

$$\tau(T) = \frac{1}{k_\mathrm{R} + k_\mathrm{NR}(T)}, \tag{2}$$

where k_R represents the radiative transitions and k_NR the temperature dependent non-radiative transitions.

For some phosphors including SCASN:Eu^{2+}, a biexponential decay behavior can be observed, resulting in two different decay times. The temperature dependence is only pronounced for the faster decay, so we used an evaluation window covering 80 ns–500 ns after the maximum signal. This approach goes back to a procedure described in detail by (Brübach et al. 2009) and (Eldridge 2019).

Besides the temporal changes of the emission intensity, spectral changes can occur. With an increasing temperature, a shift and a broadening of the emission spectrum can be observed. With increasing temperature, higher vibrational levels are populated, leading to a broadening of the emission band via electron–phonon interaction (Abram, et al. 2018). In such electronic transitions, the position of the excited state strongly depends on the crystal field, which experiences thermal expansion in case of a change in temperature. For most semiconductors, the bandgap—as the energetic distance of valence and conduction band—tends to decrease with an increase in temperature, with contributions from electron–phonon coupling and lattice expansion. As a result, the emission spectra shift towards longer wavelengths. However, for some phosphors including SCASN:Eu^{2+}, a blue-shift towards shorter wavelengths with increasing temperature can be observed. In this case, anisotropic thermal expansion can have a complex effect on the position of the emission peak, which may be responsible for this blue-shift (Abram, et al. 2018).

For thermometry, two spectral bands of the emission spectra are analyzed, ideally with an opposing temperature dependence for maximum temperature sensitivity. The intensity signal is integrated over the specified wavelength λ ranges and the ratio R between these two values is calculated as (Fuhrmann et al. 2013)

$$R = \frac{\int_{\lambda_1}^{\lambda_2} I(\lambda)\mathrm{d}\lambda}{\int_{\lambda_3}^{\lambda_4} I(\lambda)\mathrm{d}\lambda} \tag{3}$$

Both changes of the emission spectra (i.e., temporal and spectral) can be used to measure the temperature with the decay time (PDT) and the intensity ratio (PIR) method, respectively.

3 Materials and methods

In this section, details about the LOHC-phosphor system, the preparation of the catalyst and the experimental and optical setup are provided. Additionally, the recording and timing schematics as well as the post processing are laid out. For the calibration and hydrogen release measurements a self-developed measurement cell was used, which is described in detail in previous work (Bollmann, et al. 2023).

3.1 LOHC system and phosphor particles

For the loading of H0-DBT with hydrogen, a suitable catalyst, a pressure level of 1 MPa to 5 MPa and a temperature level between 423 and 573 K have been applied and are typical conditions for loading of this LOHC (Dürr, et al. 2021; Willer, et al. 2024). Throughout this process about 9 $\mathrm{kW_{th}\ kg_{H2}^{-1}}$ of heat is generated at reaction temperature (Jorschick et al. 2019; Wunsch et al. 2020). In general, the hydrogen-rich H18-DBT together with its hydrogen-lean counterpart H0-DBT form a closed-loop-cycle for the transport of hydrogen. In 1 L of H18-DBT about 56.6 g of hydrogen are stored, which corresponds to 2.05 kWh of energy in 1 kg of H18–DBT (Wunsch, et al. 2020). The endothermic dehydrogenation reaction requires a catalyst (typically Pt on AlOx), heat (about 9 $\mathrm{kW_{th}\ kg_{H2}^{-1}}$), typically at a temperature level between 553 and 593 K and a low pressure level of 0.1 MPa to 0.5 MPa (Do 2019; Wunsch, et al. 2020) (Müller et al. 2015).

The phosphor applied is a commercial SCASN:Eu^{2+} powder, which was supplied by Lumileds Germany GmbH (the doping concentration is proprietary) and is stored in a dried and evacuated condition. The phosphor particles' shape with a mean diameter of about 12 µm can be seen in the scanning electron microscopy image in (Hertle, et al. 2020). In this size class it can be assumed that the phosphor

particles follow the flow of the relatively highly viscous LOHC within dehydrogenation reactors, which will become important in possible applications in flow-through reactors. The particles are added to the fluids H0-DBT and H18–DBT with a concentration of 200 mg l^{-1}. A separate study on the phosphor concentration revealed no significant difference between values of 100 mg l^{-1} to 800 mg l^{-1} regarding the resulting decay times and intensity ratios. After adding the particles, the probe was placed in an ultrasonic bath for 5 min to ensure homogeneous dispersion. Throughout the experiments, agglomeration of the particles was observed, which will be discussed in detail in an upcoming section. SCASN:Eu^{2+} has a high quantum efficiency, a very broad excitation band ranging from 200 nm to about 550 nm, and an emission peak centered at about 620 nm. The phosphorescence lifetime lies in the range of a few hundred nanoseconds (Hertle, et al. 2020; Pust et al. 2014). To avoid absorption of the laser in the LOHC system a wavelength of 532 nm was used in present work. The phosphorescence emission exhibits a blue-shift and a decreasing decay time with increasing temperature. This behavior allows for a temperature determination based on both the PIR method and the PDT methods. The results in (Bollmann, et al. 2023) for the PDT and PIR measurements showed that SCASN:Eu^{2+} allows measurements in LOHC systems between 423 and 598 K.

3.2 LOHC catalyst preparation

For this study aluminum plates were used as a substrate for a platinum/ aluminum oxide Pt/ Al_2O_3 catalyst. The plate material was an $AlMgSi_{0.5}$ aluminum alloy (EN AW-6060, 3.3206). Sample plates of 14 mm times 10 mm and a thickness of 2 mm were cut out, with a small handle of 1 mm thickness and 4 mm length pointing away from the plate (Fig. 1). For better adherence of the layer, the plates were sandblasted, which generated a rough surface. The plates were cleaned with acetone, soap water and deionized water to remove any residuals and fatty deposits that could cause worse contact and would lead to a detaching of the layer.

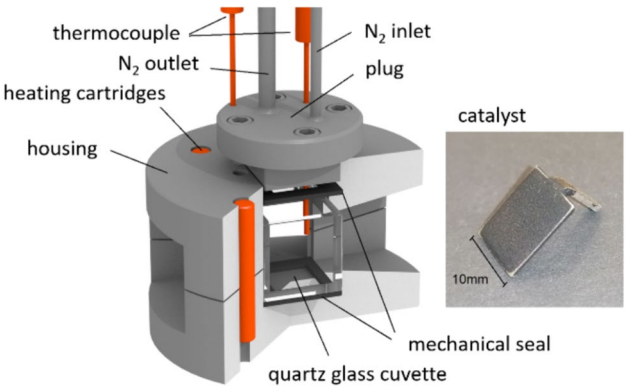

Fig. 1 Drawing of the measurement cell and a picture of the applied aluminum plate coated with a Pt/ Al_2O_3 catalyst

On the clean metal plates, a support layer was deposited with a dip-coating technique, which is described in (Solymosi et al. 2021). This method uses a mixture of aluminum oxide particles with an average diameter of 45 µm (Puralox, Sassol) and boehmit (Al_2OOH, Dispersal, Sassol) as precursor dispersed in deionized water. The boehmite was, comparable to a sol–gel approach, solved in the water and acts as a binder, building bonds to the oxide. Nitrous acid (69%) was added to control the pH and by that the properties of the resulting layer. The composition of the coating dispersion is shown in Table 1. After dispersing the aluminum oxide, the boehmite was added and mixed with a magnetic stirrer at 800 rpm for 1 h. The nitrous acid was added and the dispersion was continuously stirred for another 3.5 h.

The plates were fixed on a bar that was connected to a linear actuator (SMC 300, Movetec GmbH), which moved the plates vertically. This bar was used to dip the plates into the dispersion, which was placed under the plates in tubular containers. Quickly after placing the dispersion, the plates were dipped into the containers. For better adherence, a first step was performed with a primer dispersion that had a reduced concentration of aluminum oxide particles (primer dispersion, Table 1). The retreating velocity was set to 3 mm s^{-1}. Four repetitions with the coating dispersion (Table 1) were made, in between which the resulting layer was dried in a 323 K air stream. The coated plates were dried and subsequently placed in a muffle furnace, in which they were calcinated at 723 K in air. By weighing before and after the coating, it could be determined that the mass of deposited aluminum oxide was approx. 30 mg.

The active component was added by a wet impregnation method. A 0.1 mg_{PSA} mg^{-1} aqueous platinum sulfidic acid solution (PSA, ABCR GmbH & Co KG, CAS: 61420-92-6, 16.4 wt-% Pt) was prepared by dilution in ultra-pure water (Millipore, Thermo Fischer). The plates were immersed and moved to an orbital shaker. The platinum amount adsorbed onto the substrates was determined by the difference of

Table 1 Composition of the dispersion used in the dip-coating

Component:	Composition:	
	Primer dispersion wt.-%	Coating dispersion wt.-%
Aluminum oxide	5.76	12.00
Boehmite	2.88	2.40
Nitrous acid	3.58	3.58
AIPO	–	–
Water/ Ethanol	87.78	82.02

platinum mass in the impregnation solution before and after the impregnation. The platinum mass was measured by optical emission spectrometry using an inductively coupled plasma (ICP-OES). With regard to the geometric area of the plates the platinum loading of the evaluated catalysts was approx. 0.8 $mg_{Pt}\,cm^{-2}$.

The platinum precursor was reduced in a tube furnace (Carbolite Gero GmbH & Co KG). It was heated to 713 K in a nitrogen stream of 450 ml min^{-1} and after reaching the reduction temperature, 50 ml min^{-1} of hydrogen were added. After two hours the oven was cooled to room temperature and the plates were removed. The resulting coated plate is shown in Fig. 1.

3.3 Experimental setup

The optical setup for the planar PDT and PIR measurements of SCASN:Eu^{2+} seeded into the fluids H0-BT and H18-DBT is shown in Fig. 2.

For excitation the second harmonic (532 nm) of a pulsed Nd:YAG laser (Quantel Q–smart 450) with a pulse duration of 6 ns, a repetition rate of 10 Hz and a laser power of 5 mJ was used. The laser power was adjusted using a λ/2–plate (WPH05M-532, Thorlabs Inc.) in combination with a polarizing beamsplitter (05BC15PH.3, Newport Corporation) and monitored by a power meter (QE50LP-S-MB-D0, gentec-eo Inc.) after 50% of the laser energy was directed through a plate beam splitter (BSW10, Thorlabs Inc.). Along the optical path two highly reflective mirrors (NB07-K13, Thorlabs Inc.) and a set of three cylindrical lenses (LJ1363L2-A, LK1419L1-A, LK1487L1-A, Thorlabs Inc.) were utilized to form a light sheet with a thickness of about 0.5 mm and a height of 10 mm in the measurement volume.

The measurement cell contained the LOHC and SCASN:Eu^{2+} mixture. For the planar temperature measurements during hydrogen release the catalyst plate can be fixed to the plug of the cell. In this way, in addition to performing the calibration measurements without the catalyst, the cell also serves as a model dehydrogenation unit for hydrogen release from H18-DBT in presence of the catalyst plate. The latter can be easily substituted and thus enables the investigation of different catalyst configurations in future investigations. Temperature was varied between room temperature and a maximum of 598 K in 25 K increments. A magnetic stirrer ensured homogeneous conditions. Here, it should be mentioned that the glass cuvette can only withstand moderate heating rates of a few Kelvin per minute, making the entire procedure quite time-consuming. The installed calibrated type K thermocouples (accuracy ± 1.5 K) at the top and the bottom of the cell showed a maximum gradient of less than 1.5 K for all measurements and serve as a reference for the calibration measurements.

The emissions from the SCASN:Eu^{2+} dispersed in the LOHC system H0-DBT/H18-DBT were detected using an intensified sCMOS camera (Imager sCMOS, LaVision GmbH) and a high speed intensifier (IRO X,

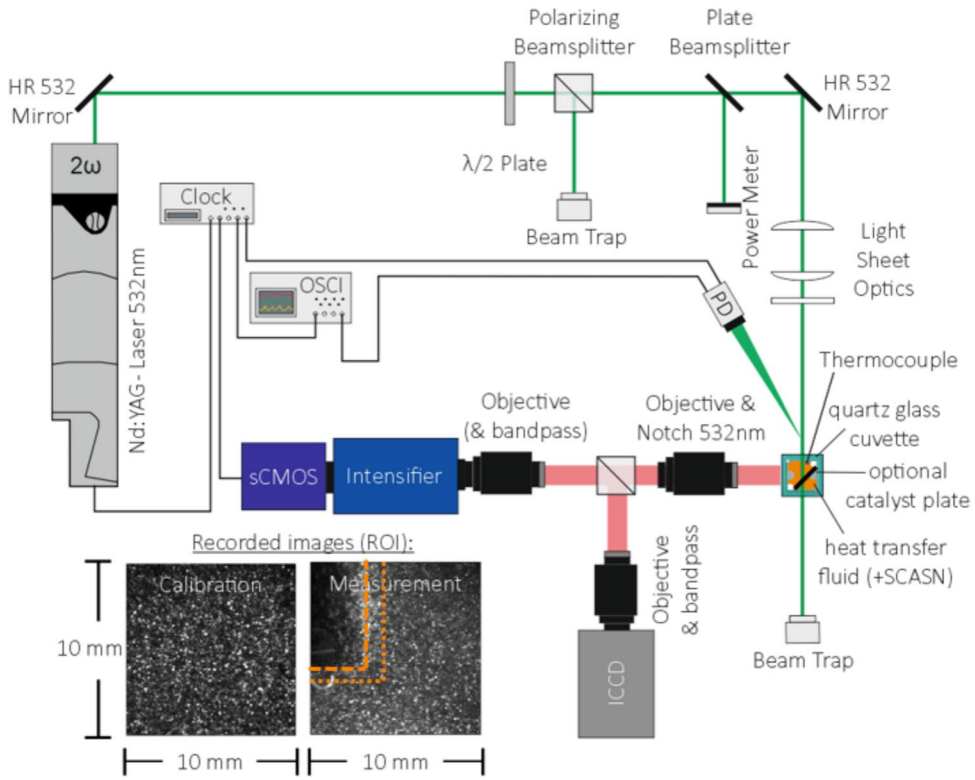

Fig. 2 Optical setup for the 2D temperature calibration and hydrogen release measurements by the decay time (PDT) and two color (PIR) methods using the SCASN:Eu^{2+} dispersed in the LOHC fluids H0-DBT and H18-DBT. Raw images are shown for calibration and hydrogen release measurement conditions with a dashed line marking the catalysts surface and a dotted line beyond which the evaluated region begins

Phosphor P46, LaVision GmbH). The mentioned system enables the acquisition of two consecutive images at a very short time interval of a minimum of ~ 300 ns with an exposure time of 60 ns for the PDT method. The signal is directed via a lens (UV-NIKKOR, 105 mm, Nikon Europe B.V) to the intensifier. The detection system is additionally equipped with a lens (SOLIGOR C/D MACRO MC 90 mm f2.5, Sun Optical Co. Ltd.) for an appropriate magnification. A 532 nm notch filter (NF533-17, Thorlabs Inc.) suppresses scattering or stray light contributions from the laser and protects the camera system from damage.

For the PIR-method in a sequential recording, an additional ICCD camera (DiCAM pro 12 bit) equipped with a longpass filter with a cutoff wavelength at 615 nm and a second objective lens (UV-NIKKOR, 105 mm, Nikon Europe B.V) was used simultaneously to the first image of the sCMOS camera. In that case, the sCMOS camera was equipped with a second bandpass filter 400 nm to 600 nm to enable the PIR method. The ICCD camera has fewer numbers of pixels compared to the sCMOS camera making the results of the PIR approach a little bit coarser compared to spatial temperature distributions based on PDT. Simultaneous recordings of both methods are in principle possible but were not applied in this case due to low signal-to-noise ratios (SNR) in the second image of the PDT approach after installation of the bandpass filter. The spectral responses of both detection channels were calibrated using a lamp (HL-3P-Cal, Ocean Optics) with known spectral irradiance. Pixel to pixel variations were investigated using an integrating sphere and a flat field correction. The determination of the temperatures via the planar decay time method was performed analogously to the procedure shown in the literature (Someya 2021; Sutton et al. 2019). To avoid interference of fluorescence or scattering signals, the detection was delayed and gated 70 ns after the laser pulse. This was found to be an optimal choice for the LOHC/phosphor system in previous work (Bollmann, et al. 2023) and constitutes a reasonable trade-off between sufficient signal intensities and fluorescence suppression (Mendieta et al. 2019). The resulting trigger scheme is shown in Fig. 3.

In case of PDT measurements, two images within one decay are recorded. The temporal distance was varied in a range between 300 and 750 ns to find the optimum between signal intensity and intensity difference. Based on the achievable sensitivities and temperature resolutions, a separation of 300 ns was shown to be advantageous. The timing of all devices was controlled with a timing unit and appropriate software DaVis (LaVision GmbH). To precisely control and adjust the timing of all components, a photodiode was used to detect the laser pulse. An oscilloscope was used to monitor and visualize all trigger signals and the photodiode's response.

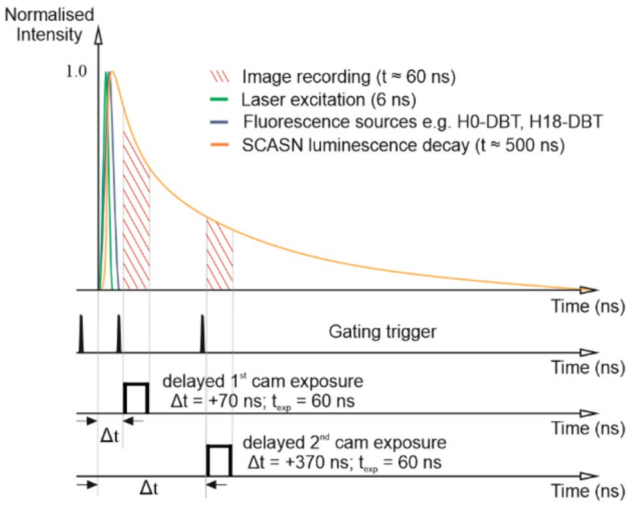

Fig. 3 Schematic representation of the luminescence signals and the detection timing strategy for planar temperature measurements using the PDT method. The duration of the excitation laser (green), the LOHC fluorescence signal (blue) and the SCASN:Eu^{2+} luminescence decay at room temperature (orange) are displayed

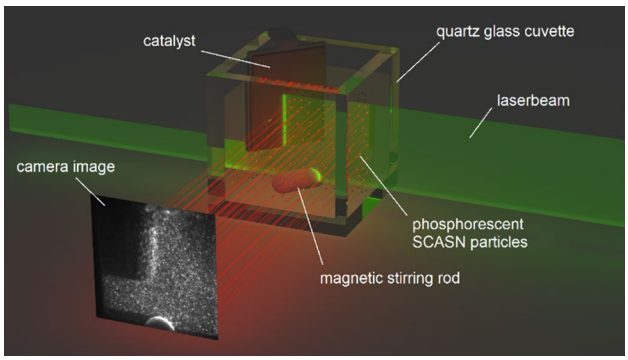

Fig. 4 Optical path during the hydrogen release measurements using a pulsed 532 nm laser light sheet exciting SCASN:Eu^{2+} particles dispersed in H18-DBT, a plate coated with catalyst, a magnetic stirrer for homogeneous temperature and particle distribution and an intensified sCMOS camera for signal detection

To check the observed results, the PIR method was additionally applied. Here, the first image of the sCMOS camera was synchronized to the ICCD camera.

3.4 Post-processing of the raw images

The optical path of the laser light sheet and the particle excitation and emission during the temperature field measurements is shown in Fig. 4. The laser beam enters the cuvette from the right side and excites the dispersed SCASN:Eu^{2+} particles located in a vertical plane. In case of measurements during hydrogen release, a catalyst plate is placed inside the cuvette, cutting the laser beam and

tilted at a 45° angle. The resulting phosphorescence emissions, displayed in red, are captured by the cameras. For the calibration measurements the catalyst is removed so no reaction is taking place. The detected signal might suffer multiple scattering effects from phosphor particles between the laser sheet and the detection setup. Therefore, a structured laser illuminated planar imaging (SLIPI) approach using a Ronchi ruling (Edmund Optics) was realized but revealed no significant difference to the conventional imaging. To maintain a good signal-to-noise ratio and spatial resolution the SLIPI technique was not applied for the following measurements.

To measure the decay time, two images within one decay process were recorded, while, to measure the change in the emission spectra, two spectral bands, defined by two optical filters were recorded with two different cameras at the same time. As the intensity below 600 nm increases and that above 600 nm slightly decreases with higher temperature, each camera captures one of these areas, resulting in two images with an opposing temperature dependence on intensity and maximum sensitivity.

In both cases, there are two images with different intensities as shown in Fig. 5 top left and right. Unless otherwise stated, 30 images were taken for each calibration measurement and averaged. After the subtraction of the background signal, the ratio of the intensity of every pixel of the two images is calculated (Fig. 5 bottom left). To exclude effects of sensor non-linearity and varying pixel to pixel sensitivity, experiments were performed with homogeneous and changing light intensities using multiple neutral density filters and a homogeneous LED panel as well as an integrating sphere similar to the approach shown in (Bauer et al. 2023; Williams and Shaddix 2007). During the final measurements, care was taken to illuminate the camera only moderately in order to remain outside the non-linear range (at highest intensities). The ultimate correction was based on the integrating sphere data but only showed minor importance due to the strategy described. To calculate the two-dimensional

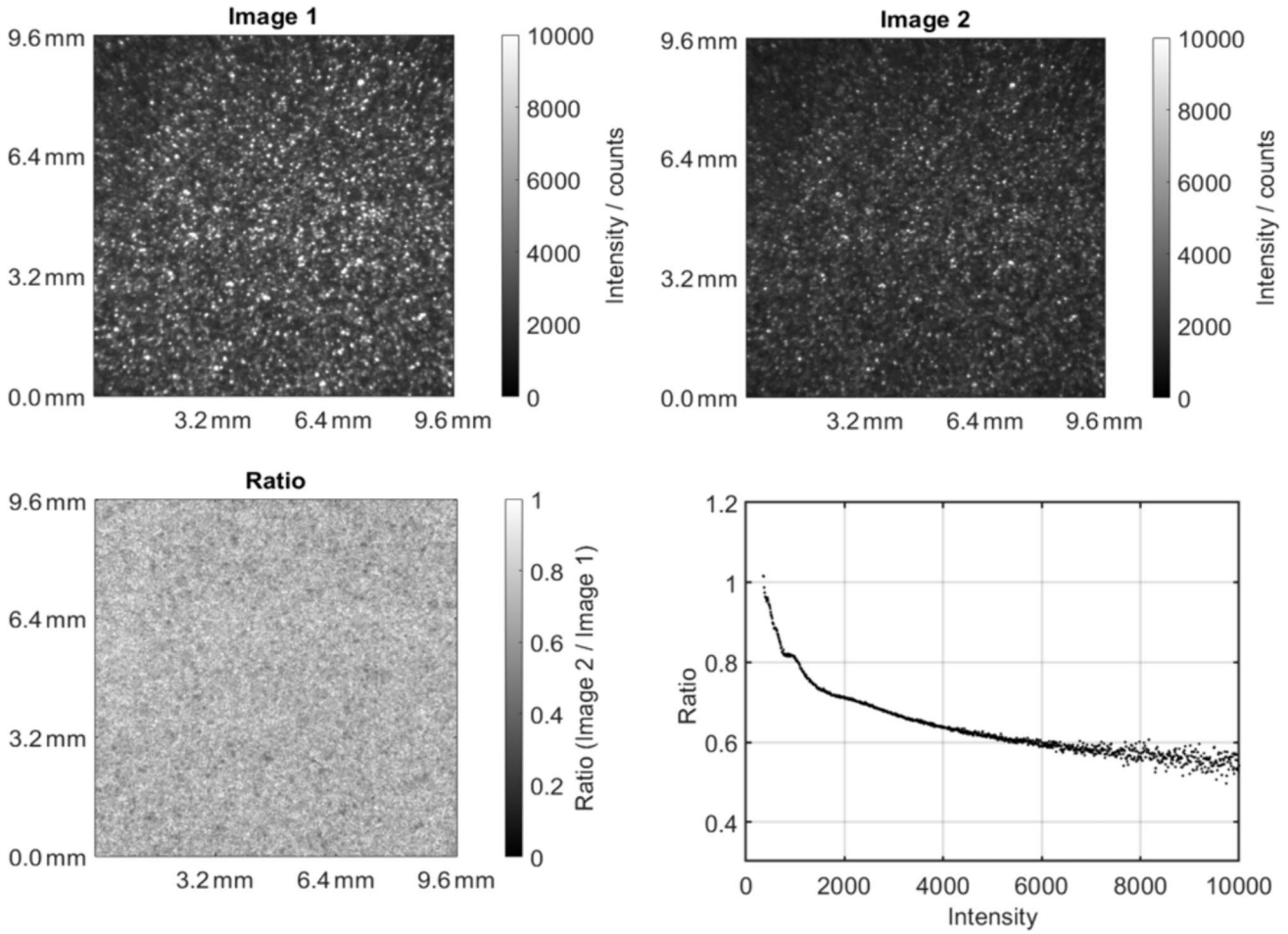

Fig. 5 Workflow of image processing of the PDT (shown) and analogously PIR method starting with two raw images with different intensities (top left and right) and the calculation of the ratio image (bottom left) leading to the investigation of the intensity dependency of the ratio (bottom right)

temperature fields only areas of the image that contain the phosphor particles can be used for the evaluation, which will be addressed by applying an intensity threshold explained in detail in the following.

It turned out that a straightforward temperature determination based on the relation between the intensity ratio and temperature was not very accurate, as the bright particles appeared to be significantly hotter than the darker particles. Here, lower ratio values result in higher temperatures for the PDT method, while for PIR it is the opposite. A possible heating effect through the laser pulse could be excluded by measurements with different pulse energies at the same temperature. A laser fluence variation using values of 15 mJ cm^{-2}, 30 mJ cm^{-2} and 45 mJ cm^{-2} showed almost no effect on the intensity ratio with a minimum and maximum deviation of 4.6% around the mean for all fluences for the PDT method. A fluence of 30 mJ cm^{-2} was chosen for the following investigations. On the other hand, further investigations demonstrated a clear correlation between the intensity ratio and the pixel intensity as shown in Fig. 5 bottom right. The higher the pixel intensity, the lower the intensity ratio, resulting in a falsely higher temperature of bright particles.

The decrease of the ratio with increasing signal intensity seems to be caused by the agglomeration behavior of the particles. The exact mechanism is unclear, however, multiple scattering (between the particles of the agglomerate) or reabsorption and lasing may be important, which are known to occur for high particle concentrations and in bulk materials (Aldén et al. 2011; Fond, et al. 2019b). In order to compensate for the intensity dependence of the ratio, the temperature was not only calibrated over the ratio, but also over the pixel intensity, resulting in a three-dimensional calibration surface. For the exemplary case of PDT, the temperature value from one specific pixel in the image can be obtained from the two input parameters: (1) intensity value of the first image and (2) the value of the ratio and use the calibration surface subsequently. This look up table method allows for the conversion of ratio to temperature images. The ratio intensity plot can also be used to analyse the minimum intensity above which the ratio is temperature sensitive. Pixels with an intensity below 2,000 counts showed no temperature sensitivity (which will be discussed in more detail in an upcoming section), so that the intensity threshold was set to 2,000 counts. Once the temperature image is obtained, pixels in the image which were below the threshold are filled by a Gaussian interpolation and smoothing filter between the temperatures of neighboring pixels. This decreases the resulting spatial resolution. which is assessed to be around 0.5 mm.

4 Results and discussion

The subsequent section describes the determination of a calibration strategy first, followed by a test case for the validity of the calibration procedure and hydrogen release measurements using the PDT and PIR methods. A comparison between both techniques allows for a cross-check of the results obtained.

4.1 Calibration measurements

The intensity calibration curves for each temperature are shown in Fig. 6 left. These measurements were repeated six times (for H0-DBT and H18-DBT) and their average is

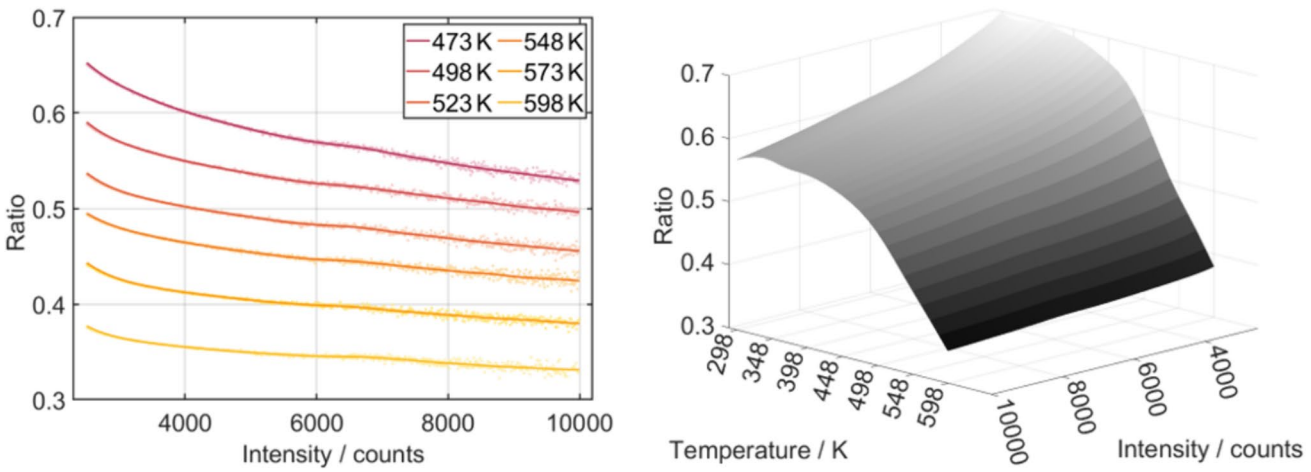

Fig. 6 Intensity-dependent calibration curves for each temperature level using the PDT-method and the phosphor SCASN:Eu^{2+} dispersed in H0-DBT on the left. Corresponding calibration surface in the temperature range between 298 and 598 K and in the intensity range between 2,000 counts and 10,000 counts –averaged over all measurements in H0-DBT and H18-DBT on the right

shown as a 3D surface in Fig. 6 right. This means that the calibration surface results from an average of the measurements in both liquids. This calibration surface was used to calculate the temperature at every pixel depending on both ratio and intensity.

The PDT calibration area of SCASN:Eu^{2+} is temperature sensitive in a range between 473 and 598 K and in the signal intensity range between 2,000 counts and 10,000 counts. The surface enables an assignment of the spatially resolved ratio values obtained via the measurement to the corresponding temperature values and thus a temperature field measurement during the hydrogen release reaction. The range of intensity ratios and the temperature sensitivity (in form of the slope of the curves in Fig. 6) are larger for smaller particles (leading to, e.g., ~ 4,000 counts) compared to larger particle agglomerates (leading to, e.g., ~ 10,000 counts). This would result in large temperature uncertainties when the agglomeration effect in the signals is not compensated. As an example, the sensitivities are 0.37% K^{-1} (3000 counts), 0.25% K^{-1} (9500 counts) for the highest ratios and 0.57% K^{-1} (3000 counts), and 0.52% K^{-1} (9500 counts) for the lower ratios. As the curves slightly flattens with increasing intensity the sensitivity decreases as well.

To elucidate the effect of agglomeration of the individual SCASN:Eu^{2+} particles in the LOHC system at specific temperatures, additional measurements were performed. Figure 7 shows the phosphorescence signals of the particles in LOHC H18-DBT for various temperatures. At 373 K the agglomeration of the particles begins revealing fewer bright spots, but with larger luminescence intensities, which then decreases again with increasing temperatures. In previous investigations, indications of similar behavior were already found for other phosphors (Hertle et al. 2018, 2017). This agglomeration behavior may have an impact on the intensity ratio and could be the reason for the intensity ratio and decay time dependencies shown above.

The evaluation of the ratio image obtained by the PIR method also showed a dependency on the pixel intensity (or particle size, respectively). With increasing intensity, the ratio value doubled in the considered intensity range. Consequently, a calibration surface was also used for the PIR method. While, the PDT method only showed a distinct temperature sensitivity at temperatures above 473 K, the intensity ratio obtained by the PIR method is sensitive over a much wider temperature range from 348 to 598 K. However, the data points in the PIR curves reveal a larger scatter around the mean value (especially at higher temperatures) and for that reason the PDT is the preferred choice. Figure 8 left shows the average ratio values over the pixel intensity of one calibration measurement cycle, while Fig. 8 right depicts the resulting calibration surface averaged over all six calibration measurements.

4.2 Test of calibration measurements

To test the calibration, independent sets of measurements were carried out. Again, the catalyst plate was removed so no reaction was taking place. The independent measurements were carried out using H0-DBT and H18-DBT in 25 K steps from room temperature to 598 K using the PDT approach. Between the individual measurements, a magnetic stirrer ensured a homogeneous temperature and particle distribution in the measurement volume. Each measurement in H0-DBT and H18-DBT was repeated three times for each temperature setting.

To analyze the accuracy of the measurements, temperature fields from independent measurements were calculated with the determined calibration surfaces. Since the average reference temperature is known from the

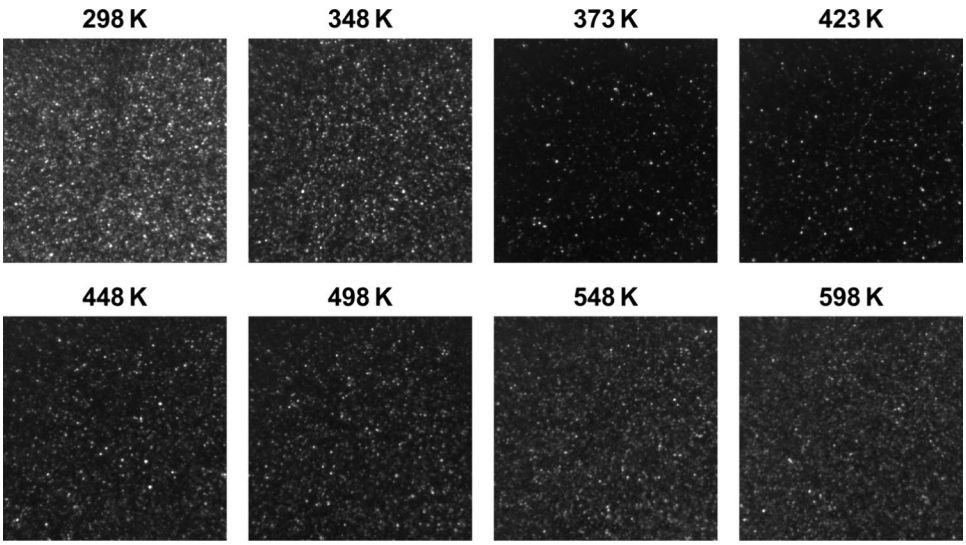

Fig. 7 Agglomeration behavior of H18-DBT during the calibration measurements for different temperature levels. A strong agglomeration can be observed at temperatures around 373 K. Signal levels are different to demonstrate the agglomeration effects on maximal intensities, the total particle concentration in the liquid is unchanged

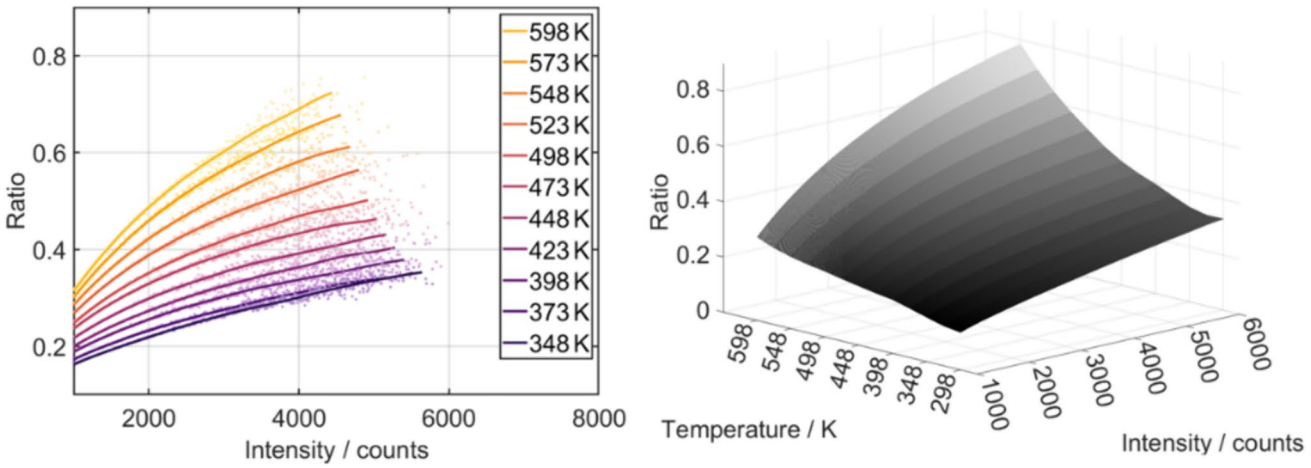

Fig. 8 Intensity-dependent calibration curves for each temperature level using the PIR method and the phosphor SCASN:Eu^{2+} dispersed in H0-DBT on the left. Corresponding calibration surface in the temperature range between 298 and 598 K and in the intensity range between 2,000 counts and 10,000 counts averaged over all measurements in H0-DBT and H18-DBT on the right

thermocouple measurements, the temperature difference between the thermocouple and the PDT temperature can be specified. Figure 9 shows single shot temperature fields in the sensitive temperature range and the resulting mean temperature $\mu(T)$ and standard deviation $\sigma(T)$ of all pixels in the image given below each image. The temperature displayed above the images is the temperature measured by the thermocouples.

For both LOHC materials, H0-DBT and H18-DBT, the single-shot result images show rather homogeneous temperature fields in the relevant temperature range between 477 and 601 K. The calculated mean temperature mostly agrees well with the temperatures measured via the thermocouples in the cuvette. Tentatively larger absolute and standard deviations are observed towards lower temperatures, where the calibration curve flattens off with the effect

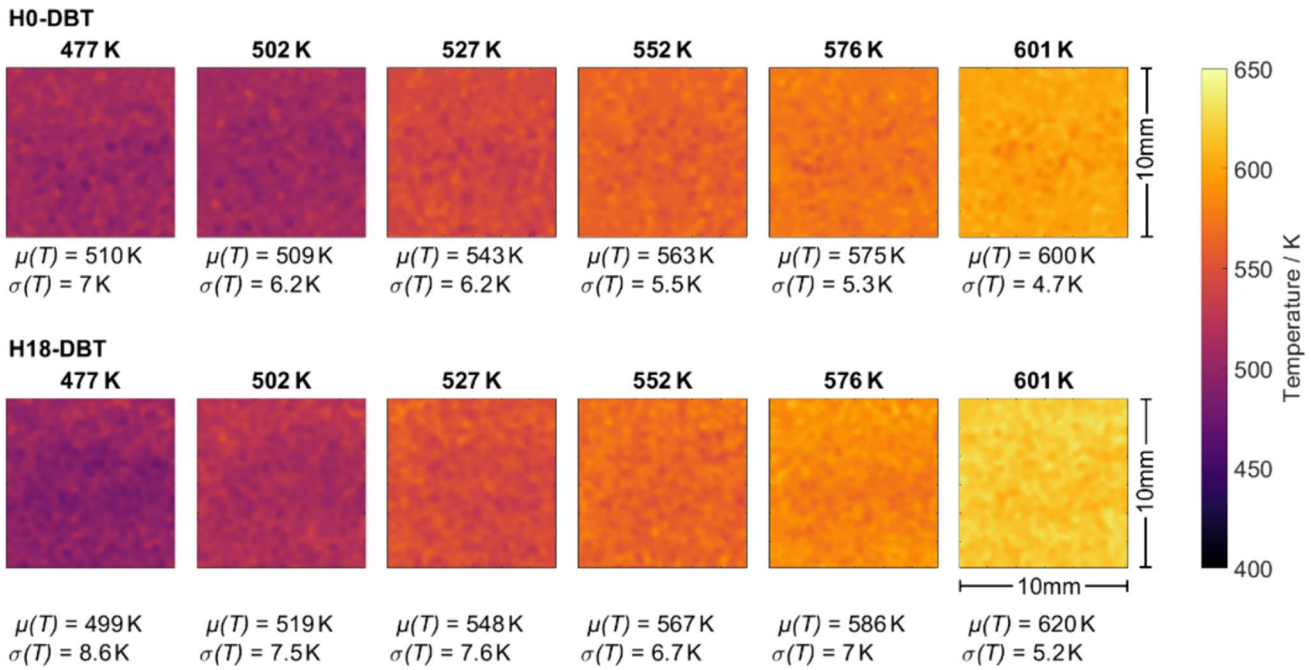

Fig. 9 Single-shot temperature fields of the evaluated measurement images of the LOHC materials H18-DBT and H0-DBT for the temperature range from 477 to 601 K using the PDT method. The temperature displayed above the images is the temperature measured by the thermocouples. The temperature value displayed below the measurement image reflects the calculated mean value. In addition, the standard deviation within each image is given

that small changes in the ratio determined may result in larger deviations.

Next, a comparison between the presented techniques may be drawn. To that end, the probability density functions (PDFs) of multiple scenarios are shown in Fig. 10 for the example cases of 575 K images without a catalyst plate in the measurement cell.

The left plot shows the difference between H0-DBT and H18-DBT based on the PDT approach. For this temperature region H18-DBT is slightly hotter than H0-DBT, which we believe is due to overall measurement uncertainty. In the center figure a comparison between PDT and PIR is shown with the latter having higher uncertainties in form of a broader PDF, which aligns with previous findings (Bollmann, et al. 2023). The right subplot of Fig. 10 depicts the impact of the chosen intensity threshold value, which affect the PDF in form of higher temperatures if the threshold value is chosen too high. While, a more thorough uncertainty analysis is prospect for a future studies, these PDFs allow for a first assessment of the impacts and uncertainties related to the techniques.

4.3 Temperature imaging during hydrogen release reaction

When the catalyst is placed in the cuvette and the temperature is higher than 500 K, the endothermic hydrogen release reaction and thus the cooling of the catalyst by the reaction starts. In order to avoid a continuous release of the stored hydrogen during the slow heating of the setup to reaction temperature (total measurement duration approx. 3 h) the cuvette is only half filled with H18-DBT so that the catalyst is hardly in contact with the LOHC. Shortly before starting the measurement, the volume is completely filled with H18-DBT, which takes the target temperature within a few tens of seconds. To avoid any unwanted oxidation processes during the heating process, the air inside the cuvette is replaced with nitrogen. To prevent the plate from heating up via the sealing plug of the measuring cell and thus to avoid faulty temperature measurement, it is thermally decoupled from the plug.

Temperature field measurements (including hydrogen release from H18-DBT) will be discussed to demonstrate the application of the technique. The first two measurements were performed with the same catalyst plate, only the LOHC material was varied between H18-DBT and H0-DBT, while all other boundary conditions were kept unchanged. Thus, for these measurements and influence of the catalyst material on the release reaction and ultimately on the resulting temperature fields can be excluded. As expected, the single shot temperature field measured for H18-DBT during the endothermic hydrogen release reaction showed a distinct cooling effect in the whole measurement volume (see Fig. 11 left). Additionally, a spot cooler by approx. 40 K could be observed right in front of the catalyst plate, where the reaction takes place, which likely results from the endothermic reaction.

In case of H0-DBT, no reaction and therefore no cooling should occur. As shown, the temperature field without hydrogen release shows no local cooling near the catalyst and an overall significantly higher temperature than for the H18-DBT case (see Fig. 11 right). The hydrogen release reaction clearly has a strong impact on the temperature and cools the catalyst as well as the whole measurement volume significantly.

To verify the results obtained by the PDT method, all measurements were repeated with the PIR method. The temperature field during hydrogen release with a target temperature of 578 K also shows temperature reduction by approx. 40 K near the catalyst, very similar to the results obtained by the PDT method (see Fig. 12).

Again, the corresponding measurement with the same catalyst but H0-DBT and thus no hydrogen release reaction showed no local cooling near the catalyst and a homogenous

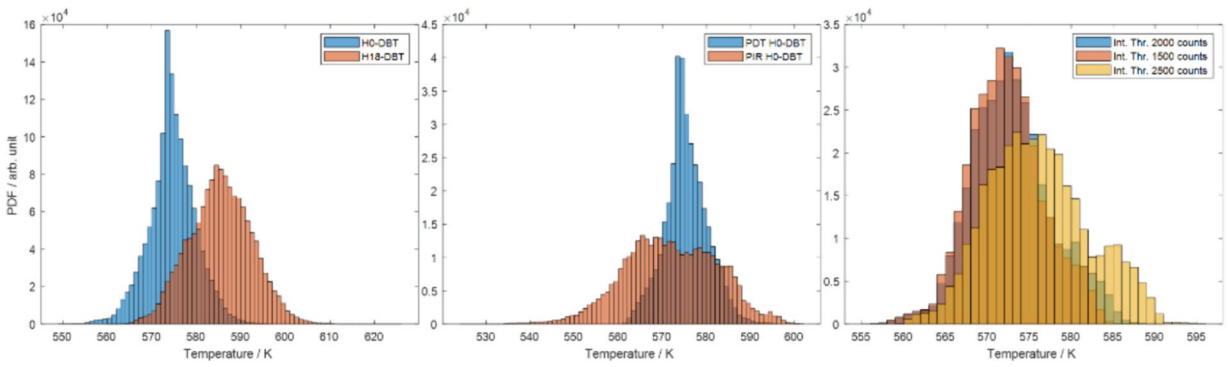

Fig. 10 Left: Comparison of PDFs for the 575 K calibration case between H0-DBT and H18-DBT determined from the PDT approach. Centre: Comparison for PDT and PIR. Right: Impact of the chosen threshold value for 1500, 2000 and 2500 counts

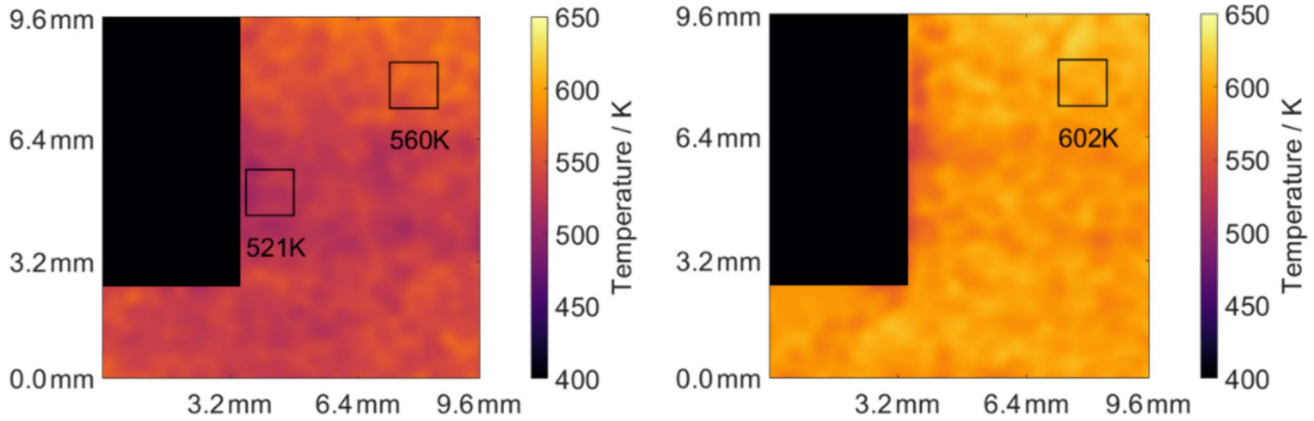

Fig. 11 Single-shot temperature field during hydrogen release from H18-DBT (left) at a target temperature of 578 K and the use of a Pt on Al_2O_3 catalyst and the temperature field of H0-DBT (right) with no hydrogen release. A cooling of the whole measuring volume due to the strongly endothermic hydrogen release reaction is clearly visible. Measurements were based on the PDT method

temperature distribution with a mean of 578 K in the region of interest similar to the PDT approach.

5 Conclusions and outlook

Temperature field determination during hydrogen release from H18-DBT by the technique of LIP using the phosphor SCASN:Eu^{2+} was successfully applied. Because of the agglomeration behavior of the SCASN:Eu^{2+} particles and the resulting intensity dependency of the decay time, a calibration surface to calibrate over both temperature and intensity was necessary and was the key to calculate accurate temperature fields with the PDT and PIR method. Both methods show approximately the same temperature distributions, whereby the sensitivity at higher temperatures (> 450 K) is better with the PDT approach, while the PIR method can still be applied for lower temperature levels. The obtained results throughout the endothermic release reaction indicate an overall cooling of about 40 K in the whole measurement volume as well as an additionally significant cooling in the region close to the catalyst surface of approx. 40 K. Thus, in future dehydrogenation reactors, the heat input should be placed in close proximity to the catalytically active and heat consuming surface. A major improvement for our measurements could be the use of a phosphor material that does not exhibit any agglomeration effects, as this facilitates the calibration procedure.

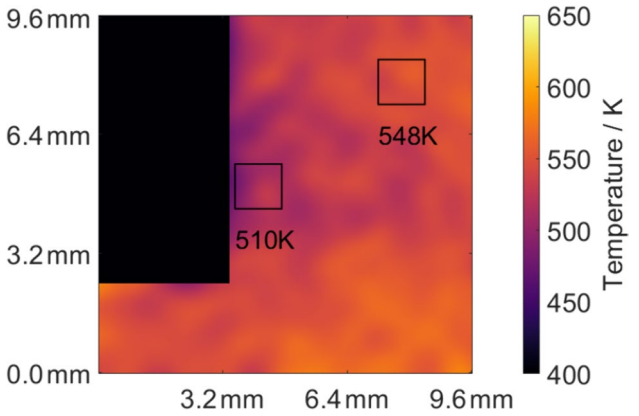

Fig. 12 Single-shot temperature field during hydrogen release using the PIR method at a target temperature of 578 K and the use of a Pt on Al_2O_3 catalyst. A temperature difference of about 40 K between the LOHC volume and near the catalyst can be observed, in agreement with the results obtained by the PDT method

The investigations show great potential for the development of reactor and process optimization strategies as well as for the validation of reaction engineering models. Furthermore, the added particles could be used in the future for the determination of flow fields during hydrogen release using simultaneous particle image velocimetry in a flow-through reactor. Additionally, in future a comparison between various catalysts materials could be drawn, which can be evaluated in a first step by the resulting temperature distributions that potentially correlate with the reaction. For more detailed insights, simultaneous measurements of the released hydrogen amount may allow for a quantification of the overall reactor efficiency.

Acknowledgements This work has been funded by the Bavarian State Ministry of Economic Affairs, Regional Development and Energy through the Helmholtz-Institute Erlangen-Nürnberg for Renewable Energy (HI ERN). We also acknowledge funding of the Erlangen Graduate School in Advanced Optical Technologies (SAOT) by the Bavarian State Ministry for Science and Art. Furthermore, we thank our colleagues Thomas Dressel, Peter Demmelmeyer and Yogeshwar Nath Mishra for supporting the measurements.

Author contributions J.B., F.B., L.Z., and S.W. conceived the study, N.H. prepared the catalyst plates, J.B. and S.K. conducted the experiments, J.B., F.B., and S.K analyzed the data, L.Z. and S.W. supported

in the interpretation of the data, J.B., F.B., S. K. and N.H. wrote the original draft of the manuscript, L.Z., P.W., and S.W. supervised the work, provided funding and edited the manuscript, S.K., J.B., and F.B. prepared the figures. All authors reviewed the manuscript.

Funding Open Access funding enabled and organized by Projekt DEAL.

Data availability No datasets were generated or analyzed during the current study.

Declarations

Conflict of interest The authors declare no competing interests.

Ethical approval Not applicable.

References

Abram C, Fond B, Beyrau F (2018) Temperature measurement techniques for gas and liquid flows using thermographic phosphor tracer particles. Prog Energy Combust Sci 64:93–156. https://doi.org/10.1016/j.pecs.2017.09.001

Abram C, Pougin M, Beyrau F (2016) Temperature field measurements in liquids using ZnO thermographic phosphor tracer particles. Exp Fluids 57:1–14. https://doi.org/10.1007/s00348-016-2200-2

Abram C, Wilson Panjikkaran I, Ogugua SN, Fond B (2020) ScVO4:Bi^{3+} thermographic phosphor particles for fluid temperature imaging with sub-°C precision. Opt Lett 45:3893–3896. https://doi.org/10.1364/OL.392088

Aldén M, Omrane A, Richter M, Särner G (2011) Thermographic phosphors for thermometry: a survey of combustion applications. Prog Energy Combust Sci 37:422–461

Bauer FJ, Braeuer PA, Wilke MW, Will S, Grauer SJ (2023) 2D in situ determination of soot optical band gaps in flames using hyperspectral absorption tomography. Combust Flame 258:112730

Beyrau F, Fond B, Abram C (2021) A summary of new developments in phosphor thermometry. Meas Sci Technol 32:120101. https://doi.org/10.1088/1361-6501/ac274e

Bollmann J, Hickl F, Preuster P, Zigan L, Wasserscheid P, Will S (2023) Phosphor thermometry in heat transfer fluids and liquid organic hydrogen carrier systems using (Sr,Ca)$SiAlN_3$:Eu^{2+}. Meas Sci Technol 34:035206. https://doi.org/10.1088/1361-6501/acaa4b

Bollmann J, Schmidt N, Beck D et al (2022) A path to a dynamic hydrogen storage system using a liquid organic hydrogen carrier (LOHC): Burner-based direct heating of the dehydrogenation unit. Int J Hydrog Energy 48:1011–1023. https://doi.org/10.1016/j.ijhydene.2022.09.234

Brübach J, Janicka J, Dreizler A (2009) An algorithm for the characterisation of multi-exponential decay curves. Opt Lasers Eng 47:75–79

Brübach J, Patt A, Dreizler A (2006) Spray thermometry using thermographic phosphors. Appl Phys B 83:499–502. https://doi.org/10.1007/s00340-006-2244-8

Bruckner N, Obesser K, Bosmann A et al (2014) Evaluation of industrially applied heat-transfer fluids as liquid organic hydrogen carrier systems. Chemsuschem 7:229–235. https://doi.org/10.1002/cssc.201300426

Childs PRN, Greenwood JR, Long CA (2000) Review of temperature measurement. Rev Sci Instrum 71:2959–2978. https://doi.org/10.1063/1.1305516

Do GT (2019) Reaktionstechnische charakterisierung und katalytische funktionalisierung von additiv gefertigten reaktorstrukturen technische fakultät. Friedrich Alexander Universität Erlangen-Nürnberg

Dramićanin M (2018) Luminescence thermometry: methods, materials, and applications. Woodhead Publishing Series in Electronic and Optical Materials, Duxford

Dramićanin MD (2020) Trends in luminescence thermometry. J Appl Phys 128:040902. https://doi.org/10.1063/5.0014825

Dürr S, Zilm S, Geißelbrecht M et al (2021) Experimental determination of the hydrogenation/dehydrogenation-equilibrium of the LOHC system H0/H18-dibenzyltoluene. Int J Hydrogen Energy 46:32583–32594

Eldridge JI (2019) Luminescence decay-based Y_2O_3: Er phosphor thermometry: temperature sensitivity governed by multiphonon emission with an effective phonon energy transition. J Lumin 214:116535

Fond B, Abram C, Pougin M, Beyrau F (2019a) Characterisation of dispersed phosphor particles for quantitative photoluminescence measurements. Opt Mater 89:615–622. https://doi.org/10.1016/j.optmat.2019.01.011

Fond B, Abram C, Pougin M, Beyrau F (2019b) Investigation of the tin-doped phosphor (Sr, $Mg)_3(PO_4)_2$:Sn^2+ for fluid temperature measurements. Opt Mater Express 9:802–818. https://doi.org/10.1364/ome.9.000802

Fuhrmann N, Brübach J, Dreizler A (2013) Phosphor thermometry: a comparison of the luminescence lifetime and the intensity ratio approach. Proc Combust Inst 34:3611–3618

Fuhrmann N, Brübach J, Dreizler A (2014) On the mono-exponential fitting of phosphorescence decays. Appl Phys B 116:359–369. https://doi.org/10.1007/s00340-013-5700-2

Hertle E, Bollmann J, Aßmann S et al (2020) Characterization of the phosphor (Sr, Ca)$SiAlN_3$: Eu^{2+} for temperature sensing. J Lumin 226:117487. https://doi.org/10.1016/j.jlumin.2020.117487

Hertle E, Chepyga L, Batentschuk M, Will S, Zigan L (2018) Temperature-dependent luminescence characteristics of Dy^{3+} doped in various crystalline hosts. J Lumin 204:64–74

Hertle E, Chepyga L, Batentschuk M, Zigan L (2017) Influence of codoping on the luminescence properties of YAG:Dy for high temperature phosphor thermometry. J Lumin 182:200–207. https://doi.org/10.1016/j.jlumin.2016.10.033

Jorschick H, Bulgarin A, Alletsee L, Preuster P, Bösmann A, Wasserscheid P (2019) Charging a liquid organic hydrogen carrier with wet hydrogen from electrolysis. ACS Sustain Chem Eng 7:4186–4194. https://doi.org/10.1021/acssuschemeng.8b05778

Khalid AH, Kontis K (2008) Thermographic phosphors for high temperature measurements: principles, current state of the art and recent applications. Sensors 8:5673–5744. https://doi.org/10.3390/s8095673

Kim D, Yi SJ, Kim HD, Kim KC (2017) Simultaneous measurement of temperature and velocity fields using thermographic phosphor

tracer particles. J Visualization 20:305–319. https://doi.org/10.1007/s12650-016-0394-2
Lemoine F, Castanet G (2013) Temperature and chemical composition of droplets by optical measurement techniques: a state-of-the-art review. Exp Fluids 54:1–34
Lindén J, Knappe C, Richter M, Aldén M (2012) Precision in 2D temperature measurements using the thermographic phosphor BAM. Meas Sci Technol 23:085205. https://doi.org/10.1088/0957-0233/23/8/085205
Mendieta A, Fond B, Dragomirov P, Beyrau F (2019) A delayed gating approach for interference-free ratio-based phosphor thermometry. Meas Sci Technol 30:074002. https://doi.org/10.1088/1361-6501/ab1b0c
Modisha P, Bessarabov D (2020) Stress tolerance assessment of dibenzyltoluene-based liquid organic hydrogen carriers. Sustain Energy Fuels 4:4662–4670. https://doi.org/10.1039/d0se00625d
Müller K, Stark K, Emel'yanenko VN et al (2015) Liquid organic hydrogen carriers: thermophysical and thermochemical studies of benzyl- and dibenzyl-toluene derivatives. Ind Eng Chem Res 54:7967–7976. https://doi.org/10.1021/acs.iecr.5b01840
Preuster P, Alekseev A, Wasserscheid P (2017a) Hydrogen storage technologies for future energy systems. Annu Rev Chem Biomol Eng 8:445–471. https://doi.org/10.1146/annurev-chembioeng-060816-101334
Preuster P, Papp C, Wasserscheid P (2017b) Liquid organic hydrogen carriers (LOHCs): toward a hydrogen-free hydrogen economy. Acc Chem Res 50:74–85. https://doi.org/10.1021/acs.accounts.6b00474
Pust P, Weiler V, Hecht C et al (2014) Narrow-band red-emitting $Sr[LiAl_3N_4]:Eu^{2+}$ as a next-generation LED-phosphor material. Nat Mater 13:891–896. https://doi.org/10.1038/nmat4012
Schulz C, Sick V (2005) Tracer-LIF diagnostics: quantitative measurement of fuel concentration, temperature and fuel/air ratio in practical combustion systems. Prog Energy Combust Sci 31:75–121. https://doi.org/10.1016/j.pecs.2004.08.002
Solymosi T, Auer F, Dürr S, Preuster P, Wasserscheid P (2021) Catalytically activated stainless steel plates for the dehydrogenation of perhydro dibenzyltoluene. Int J Hydrogen Energy 46:34797–34806. https://doi.org/10.1016/j.ijhydene.2021.08.040
Someya S (2021) Particle-based temperature measurement coupled with velocity measurement. Meas Sci Technol 32:042001. https://doi.org/10.1088/1361-6501/abc0b0
Sutton G, Greenen A, Roebuck B, Machin G (2019) Imaging phosphor thermometry from T = 20 °C to 450 °C using the time-domain intensity ratio technique. Meas Sci Technol 30:044002. https://doi.org/10.1088/1361-6501/ab04ea
Teichmann D, Arlt W, Wasserscheid P (2012) Liquid organic hydrogen carriers as an efficient vector for the transport and storage of renewable energy. Int J Hydrogen Energy 37:18118–18132. https://doi.org/10.1016/j.ijhydene.2012.08.066
Teichmann D, Arlt W, Wasserscheid P, Freymann R (2011) A future energy supply based on liquid organic hydrogen carriers (LOHC). Energy Environ Sci 4:2767. https://doi.org/10.1039/c1ee01454d
van Swieten TP, van Omme T, van den Heuvel DJ et al (2021) Mapping elevated temperatures with a micrometer resolution using the luminescence of chemically stable upconversion nanoparticles. ACS Appl Nano Mater 4:4208–4215. https://doi.org/10.1021/acsanm.1c00657
Willer M, Preuster P, Geißelbrecht M, Wasserscheid P (2024) Continuous dehydrogenation of perhydro benzyltoluene and perhydro dibenzyltoluene in a packed bed vertical tubular reactor–the role of LOHC evaporation. Int J Hydrogen Energy 57:1513–1523
Williams TC, Shaddix CR (2007) Simultaneous correction of flat field and nonlinearity response of intensified charge-coupled devices. Rev Sci Instrum 78:123702
Wunsch A, Berg T, Pfeifer P (2020) Hydrogen production from the LOHC perhydro-dibenzyl-toluene and purification using a 5 microm PdAg-membrane in a coupled microstructured system. Materials 13:277. https://doi.org/10.3390/ma13020277

Authors and Affiliations

Jonas Bollmann[1,2] · Florian Bauer[1,2] · Silvan Keim[1] · Nikolas Herz[4] · Lars Zigan[1,2,3] · Peter Wasserscheid[4,5,6] · Stefan Will[1,2]

✉ Florian Bauer
florian.fb.bauer@fau.de

[1] Lehrstuhl für Technische Thermodynamik (LTT), Friedrich-Alexander-Universität Erlangen-Nürnberg (FAU), Am Weichselgarten 8, D-91058 Erlangen, Germany

[2] Erlangen Graduate School in Advanced Optical Technologies (SAOT), Friedrich-Alexander-Universität Erlangen-Nürnberg (FAU), Paul-Gordan-Str. 6, D-91052 Erlangen, Germany

[3] Present Address: Institut für Thermodynamik, Professur für Energiewandlung, Fakultät für Luft- und Raumfahrttechnik, Universität der Bundeswehr München (UniBw M), Werner-Heisenberg-Weg 39, D-85577 Neubiberg, Germany

[4] Helmholtz-Institute Erlangen-Nürnberg for Renewable Energy (IEK 11), Forschungszentrum Jülich, Egerlandstr. 3, D-91058 Erlangen, Germany

[5] Institute for a Sustainable Hydrogen Economy (INW), Forschungszentrum Jülich GmbH, Wilhelm-Johnen-Straße, D-52428 Jülich, Germany

[6] Lehrstuhl für Chemische Reaktionstechnik (CRT), Frie drich-Alexander-Universität Erlangen-Nürnberg (FAU), Egerlandstr. 3, D-91058 Erlangen, Germany